Modular Deep Learning Segmentation Algorithm for Concrete Microscopic Images

Benoit Hilloulin, Imane Bekrine, Emmanuel Schmitt, Ahmed Loukili

Modular Deep Learning Segmentation Algorithm for Concrete Microscopic Images

B. Hilloulin[1], I. Bekrine[1], E. Schmitt[2], A. Loukili[1]

[1] *Nantes Université, Ecole Centrale Nantes, CNRS, GeM, UMR 6183, ,1 rue de la Noë, 44321 Nantes, France – e-mail: benoit.hilloulin@ec-nantes.fr; imane.bekrine@ec-nantes.fr; ahmed.loukili@ec-nantes.fr*

[2] *Vicat, 4 rue Aristide Berges – Les trois vallons, 38081 L'Isle d'Abeau, France – e-mail: emmanuel.schmitt@vicat.fr*

Abstract

Segmentation procedures of concrete microscopic images and standard test methods devoted to the spacing factor calculation for the freeze-thaw resistance assessment of concrete are time-consuming and skill-dependent. Moreover, manual color treatment and careful image examination are often needed. Within the past few years, Convolutional neural networks (CNN) have proved unpreceded performances in image segmentation and object detection tasks, though they often showed limited reusability and modularity. This study introduces an open-source modular deep learning segmentation algorithm of concrete microscopic images. The algorithm is based on two CNN models dedicated to air voids and aggregates detection. The algorithm performances have been calculated using various concrete, mortar, and cement paste samples. The Protected Paste Volume (PPV) and distance-to-air-void have been computed and agreed well with the experimental spacing factor. Moreover, a better correlation between PPV and scaling was found than between experimentally measured spacing factors and scaling, highlighting a critical spacing factor interval from 200 µm to 300 µm.

Keywords: Deep Learning; Air-void analysis; Freezing and Thawing; Image Analysis; Microstructure.

1. Introduction

Concrete formulations can be adapted to withstand particular exposure conditions, and formulation guidelines are most of the time given in the standards. Nonetheless, due to its heterogeneous nature, concrete is a complex material. While its macroscopic properties have been studied for a long time, its microscopic properties, governing the macroscopic ones, are historically less studied. One of the critical properties of concrete related to its durability, especially to freeze-thaw and permeability properties, is its air-void structure [1]. Air entraining agents can be employed to control the pore size distribution and the air content of concrete to increase its durability [2–5]. The number of pores and pore size distribution also impacts the mechanical properties of concrete. Pores are usually classified depending on their diameter: gel pores (≤ 10 nm), transition pores (10nm-100nm), capillary pores (100nm-1000nm), and air voids (≥ 1000nm). The latter two are mainly due to the evaporation of free water during concrete life and created during the mixing process, respectively.

Various techniques can be used for pore structure analysis, such as mercury intrusion porosimetry, gas absorption, nuclear magnetic resonance, and electron microscopy. However, due to sample size limitations, they are hardly applicable from an industrial point of view to get the overall properties of decimeters-large concrete samples. Therefore, generally manual or time-consuming techniques are defined in the standards such as fresh state air-void content [6] and petrographic analysis based on microscopic images. The ASTM [7] and Eurocode [8] methods consist in sectioning a concrete block, the section is then polished and air voids are detected and counted visually using the help of a microscope [9]. Additional parameters like the protected paste volume can be calculated [10,11]. Several methods have been proposed to enhance the contrast between the air voids of the concrete matrix and the aggregates that is a critical issue. For example, manual color treatment (using black ink to color the surface and a white powder to fill air-voids, or a phenolphthalein-based color treatment to increase the

contrast between the paste and the aggregates) has been proved to be efficient but can be both time-consuming and skill-dependent [12–14]. Indeed, the colorant that is added to distinguish the paste and the aggregates can be trapped in some aggregate or sand particles because of their porosity or polishing defects, while the clear powder used to detect the air voids can be easily trapped in the cement paste because of bad polishing. Then, it has been shown that the image analysis process can be accelerated using automatic methods like the RapidAir 457 testing instrument [12,15]. These methods have been well documented but mostly rely on the manual or semi-automatic distinction between air voids and the remaining concrete matrix by coloration, which depends on the operator and is a critical error-prone step. This critical coloration procedure might significantly impact on the later analysis, such as automated segmentation, and leads to the loss of a massive amount of image information, as in the case of the black and white coloration procedure, which mainly requires the use of a grey-scale version of the images. For these reasons, completely automated techniques, without any coloration step, could help improve the concrete air void analysis making it faster and more reliable.

As for criterion settlement regarding air-void system quality in terms of frost-resistance, Powers' spacing factor $\overline{L}$ [3], which corresponds approximatively to the maximal distance of any point in cement paste to the edge of the nearest void, remains the most used in the normative context. It is commonly considered that concrete with a $\overline{L} \leq 200$ µm is freeze/thaw immune. However, several other parameters have been proposed and studied, such as the content of micropores A_{300} and the protected paste volume (PPV) calculated following different approaches [11,16]. In [11], the presence of aggregates was partially taken into account in calculating PPV by subtracting the area of aggregates on protected paste calculated images. A comparison with the spacing factor of frost-resistant concretes was conducted, and the results suggested a better correlation between the frost resistance and the PPV than

between the frost resistance and the spacing factor. The authors highlighted the need for further studies and the time-consuming and challenging segmentation procedure because of the manual preparation and microscopic examination.

Machine Learning (ML) based techniques have been applied to various Civil Engineering problems such as concrete properties predictions like strength [17], creep [18] and shrinkage [19]. Image-related problems have also been addressed for some years, from edge detection [20] to visual crack detection and monitoring [21,22] to component detection and classification [23,24] or industrial applications like helmet use detection for construction safety [25]. ML-based techniques have also been used to supplement image information by other measurements such as chemical analysis [26] indentation measurements [27,28]. Therefore, advanced image analysis techniques could help solve the issues related to air voids structure analysis and phase segmentation in concrete. In computer vision, deep learning image analysis has become popular for image analysis-related problems. Convolutional neural networks (CNN) have achieved unprecedented accuracy and efficiency in pattern recognition and semantic segmentation. Using training images, then comparing the model's error using validation images, and finally testing the model performance on a test set of images, complex CNN architectures made of successive convolutional and pooling layers have been built. For example, the Resnet architecture [29], introduced some years ago, has considerably improved CNN results in international competitions.

Recently, semantic segmentation CNN models have successfully addressed air voids detection problems in concrete materials petrographic analysis [30] [31]. These latter models exhibited good accuracy, but several major difficulties remain and need to be overcome before an eventual large-scale use. First, the semantic segmentation models inherently lack accuracy in distinguishing close instances, e.g., air voids in this problem, which is a major drawback because of the importance of the size distribution and location of air voids regarding

concrete's durability [32]. This shortcoming can be addressed using other cutting-edge CNN models like deep learning instance segmentation models such as the Mask R-CNN or the PANet model [33]. These models, based on backbones like Resnet can lead to better accuracy with a limited amount of resources because they create masks of the detected instances besides bounding boxes. Mask R-CNN [34] model has been successfully applied recently in Civil Engineering for crack inspection [35–37] after similar work done using semantic segmentation using Unet [38,39], 3D micro-tomography image analysis [40]. Various studies published up-to-date make Mask R-CNN a good candidate for industrial usage as it might show a better precision than other models such as PANet [41]. Recently, Mask R-CNN proved to be a very effective algorithm for macro-pore detection [42].

The present manuscript addresses the challenge of fast and accurate phase segmentation of concrete with the minimum amount of sample preparation and human bias-prone preparation and interpretation. The main objective is to demonstrate the potential of the instance segmentation technique as opposed to classic pixel-based techniques for air voids and aggregate detection in concrete prior to a potential industrial deployment of a modular model for cementitious materials with various microstructures: from normal strength, eventually with lightweight aggregates, concrete to ultra-high performance concrete, with different types of aggregates and eventually mineral substitutions (calcined clay, slag) to considerably change the concrete aspect and properties [43,44]. To this end, an extended dataset of concrete, mortar, and cement paste microscopic images is built to train two complementary instance segmentation models based on Mask R-CNN architecture to quickly and accurately detect air voids and aggregates, respectively. The accuracy of the trained model is quantified and validated on test images, and its versatility is demonstrated. Then, an inference strategy on large-scale concrete images is defined to study the aggregates and air void structure on real petrographic concrete slices. The model performance is discussed to highlight its benefits

and possible improvements. Finally, the Protected Paste Volume is calculated using the large-scale segmented images using a novel multi-threaded open source algorithm, and the relation with scaling-resistance is established.

2. Materials and methods

2.1 Mix designs, samples preparation, and experimental tests

2.1.1 Concrete, mortar & cement paste specimens dedicated to model training

During the training stage, 30 concrete, mortar and cement paste specimens of 12 various compositions (8 concrete, 2 mortar, and 2 cement pastes formulations) were studied. In order to cover a wide variety of air void structures, some concrete formulations included AEA, generating an important number of air voids, while others, like self-compacting concretes (SCCs) contained a limited amount of air voids. All the concrete formulations were similar to formulations used on site, some of them to design frost-resistant concrete (XF2 or XF3 according to Eurocodes) or normal to high-strength concretes with or without commonly used supplementary cementitious materials (SCM) like slag or calcined clay, giving different colors to the cement paste. Special attention was paid to the variety of the aggregates (siliceous, calcareous, granite, basalt) and their size distribution. Figure 1 illustrates the variety of the samples studied and Table 1, resp. Table 2, gives the composition of one concrete, resp. one mortar. The other formulations are not given due to confidentiality restrictions. After at least 7 days of curing, the samples were sawn in order to obtain slices: 4 x 4 x 1 cm^3 slices for cement pastes and mortars and 10 x 10 x 2 cm^3 ones for concrete specimens. The slices were then polished with SiC paper down to SiC 4000 before image acquisition described in paragraph 2.1.3.

Table 1. Example of one concrete formulation (kg/m^3)

Cement	Sand 0/4	Gravel 4/10	Gravel 10/20	Water	Superplasticizer
385	850	289	640	169	1.925

153

154 **Table 2.** Example of one mortar composition

Cement (kg/m^3)	Calcareous Sand 0/4 (kg/m^3)	Water (kg/m^3)	W/C	Paste volume (%)
566	1344	270	0.43	45

155

a)

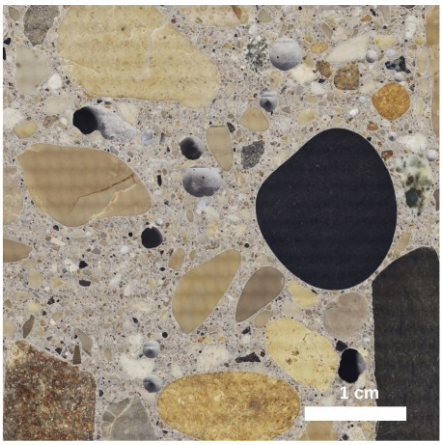

b)

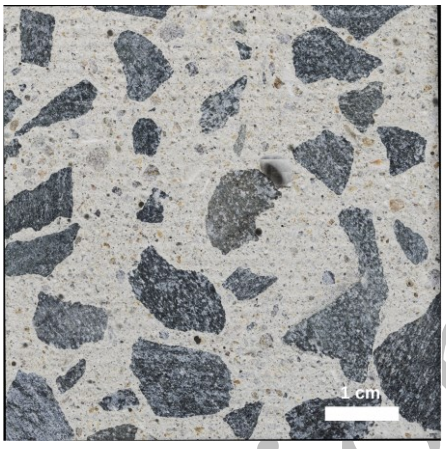

c)

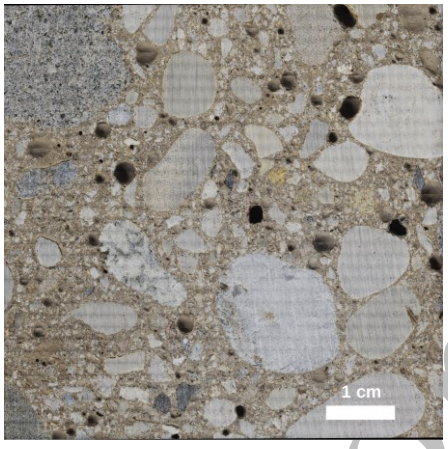

d)

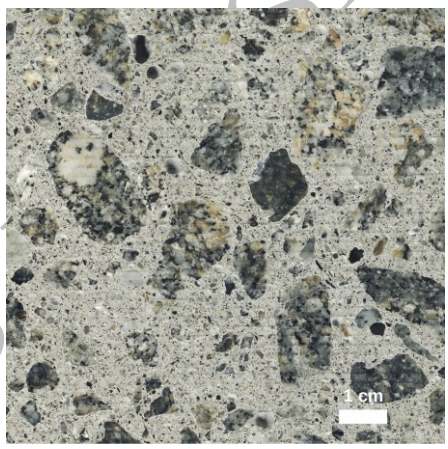

e)

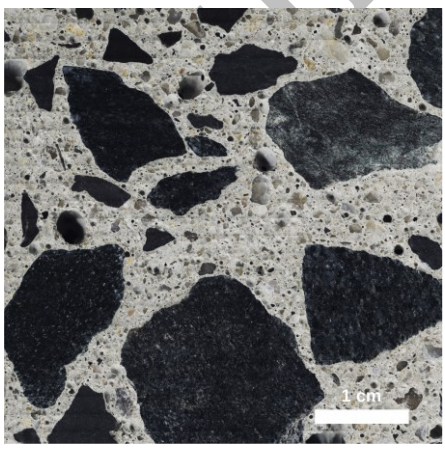

f)

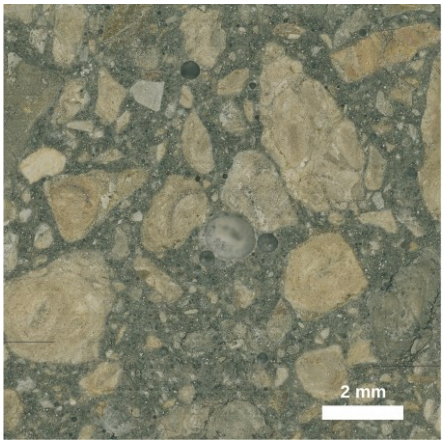

g)

h)

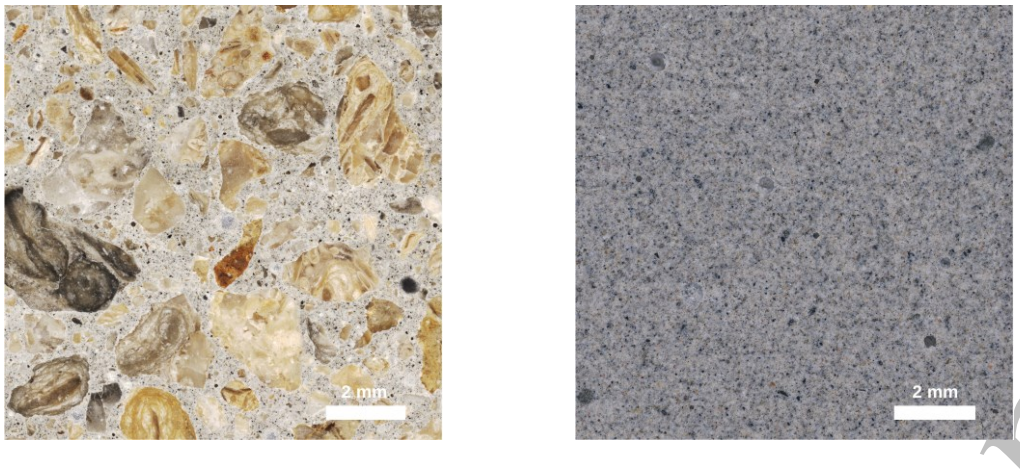

Fig 1: Overview of some samples photographs used in the deep learning instance segmentation model: a) – e) concrete samples, f) and g) mortar samples (mortars 1 and 2), h) cement paste sample (cement paste 1).

2.1.2 Specimens and experiments for model testing and validation

In order to test, validate the model and calculate the protected paste volume, concretes of 15 different formulations were prepared. The compositions are reported in Table 3). AEA was added to the mix and with various contents. Air content and slump were measured after mixing according to NF EN 12350-7 and NF EN 12350-2 standards, respectively. Concrete samples were cast in 15 x 15 x15 cm^3 molds, covered with plastic foil and cured for 1 day in 20°C and 50% relative humidity room. After 24h, the cubes were unmolded and cured in water 7 days; then some of the cubes were subjected to standard spacing factors measurements (ASTM C457 / C457M-16) and freeze-thaw tests according XP P18-420 standard, others were further cured in water until testing time. Two slices were cut from the same cubic sample to measure the standard spacing factor and the air content in the solid section. Besides, scaling was measured during 56 freeze-thaw cycles on four 15 x 15 x 7 cm^3 prisms for C1 to C4, C8, C9, C10 and C12 concretes. The measured properties are summarized in Table 4.

Table 3. Concrete compositions (kg / m^3) (add 1 and add 2 refer to admixtures, by default in kg / m^3, sometimes only in percentage relative to cement mass (%), C5a to C5d differ by the cement provider only, C6 and C7 include CEM II/A-LL 42.5N instead of CEM I 52.5 N for other concretes)

Name	Cement	Sand 0/4	Sand 0/1	Gravel 4/10	Gravel 10/20	Water	Add 1	Add 2	AEA	W/C
C1	385	795	-	244	701	171	3.08	0.963	0.193	0.42
C2	385	795	-	245	701	181	3.08	0.963	0.231	0.42
C3	350	880	-	918	-	162	2.275	0.350	0.420	0.44
C4	385	795	-	244	701	171	3.08	0.963	0.501	0.42
C5a-d	385	850	-	289	640	169	1.925	-	0.270	0.45
C6	320	537	249	310	641	172	4.160	0.640	0.128	0.50
C7	320	537	249	310	641	172	4.160	0.640	0.128	0.50
C8	385	750	-	300	760	155	0.35%	0.2%	0.13%	0.40
C9	385	768	-	421	610	165	1.06%	-	1.54%	0.43
C10	420	770	-	420*	530	170	3.4	1.58	0.75	0.40
C12	385	811	-	355	613	162	0.45%	0.1%	0.05%	0.42

* Gravel 4/16

Table 4. Slump and freeze-thaw related properties of concretes (spacing factor and air content in the solid sections are the mean values of two measurements, scaling is the mean value of four measurements)

Name	**Slump (cm)**	**Air content (%)**	**Spacing factor (µm)**	**Scaling (g/m^2)**
C1	16.0	3.6	411	2192

C2	15.0	4.0	382	3784
C3	3.0	4.5	302	3454
C4	11.0	4.5	310	561
C5a	20.7	11.6	132	-
C5b	13.5	9.8	142	-
C5c	9	9.2	154	-
C5d	10	9.14	155	-
C6	14.0	6.7	177	-
C7	17.0	5.2	258	-
C8	16.0	6.13	173	717
C9	0.35	7.93	115	542
C10	21.0	8.13	138	59
C11	18.0	5.3	259	-
C12	12.0	4.27	222	1570

2.1.3 Image acquisition of samples surface

2D maps of the sections surfaces were obtained using a Hirox RH-2000 3D microscope by merging hundreds of images evenly spaced along the section. The size of the equivalent field of vision was around 8-10 x 8-10 cm^2 for concrete samples and 3.5 x 3.5 cm^2 for cement paste and mortar samples. Magnification of x 50 was chosen according to the standard suggestion leading to final horizontal resolutions of the 2D projected image of 3.13 µm / pix. High-definition images of around 30000 x 30000 pix were finally obtained for concrete samples. Various parts of these images of samples described in paragraph 2.1.1, referenced as 'raw images' in the article, were selected to train and test the deep neural network algorithm, while images from samples described in paragraph 2.1.2 were used to test the model and compare

its results with manual spacing factor measurements and freeze-thaw resistance of the various concrete formulations.

2.2 CNN model

2.2.1 CNN model architecture

A deep learning instance segmentation model was used in order to detect circular-shape voids and polygonal-shape aggregates at a multi-pixel level. Mask R-CNN was used due to its accuracy, relatively good detection speed, and the limited number of training images needed [45]. As illustrated in Fig. 2 Mask R-CNN model is a multi-layered convolution neural network based on Tensorflow 1.14, which uses the convolution kernels to extract features and generate masks. The image is finally restored to its original size with the associated mask using upsampling strategies. Resnet-101 backbone architecture was selected due to its sensitivity.

Two separate Mask R-CNN, detecting air voids and aggregates respectively, were combined. Even though detection by a single model would be faster, the combination of two models enhances the model's modularity, and several other single models would be added to either the pore detection or the aggregate detection algorithm in the future. After training, which will be developed in the next section, detection could then be performed on the same concrete image with several resolutions from the original resolution to a 16 x smaller resolution, as illustrated in Fig. 3. Several detection results could be obtained using these two models and several input image resolutions: smaller instances (voids or aggregates) were detected using the high definition images, while larger instances were detected using lower resolution images. After detection, binary images of the detected instances were generated and merged in order to obtain a high resolution map of the air voids and a high-resolution map of the aggregates. The code is open-sourced at [46].

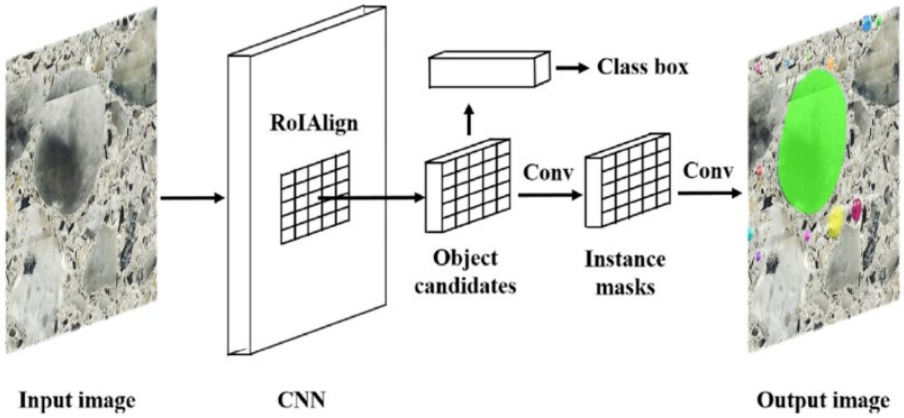

220

221 **Fig. 2.** Mask R-CNN architecture

222

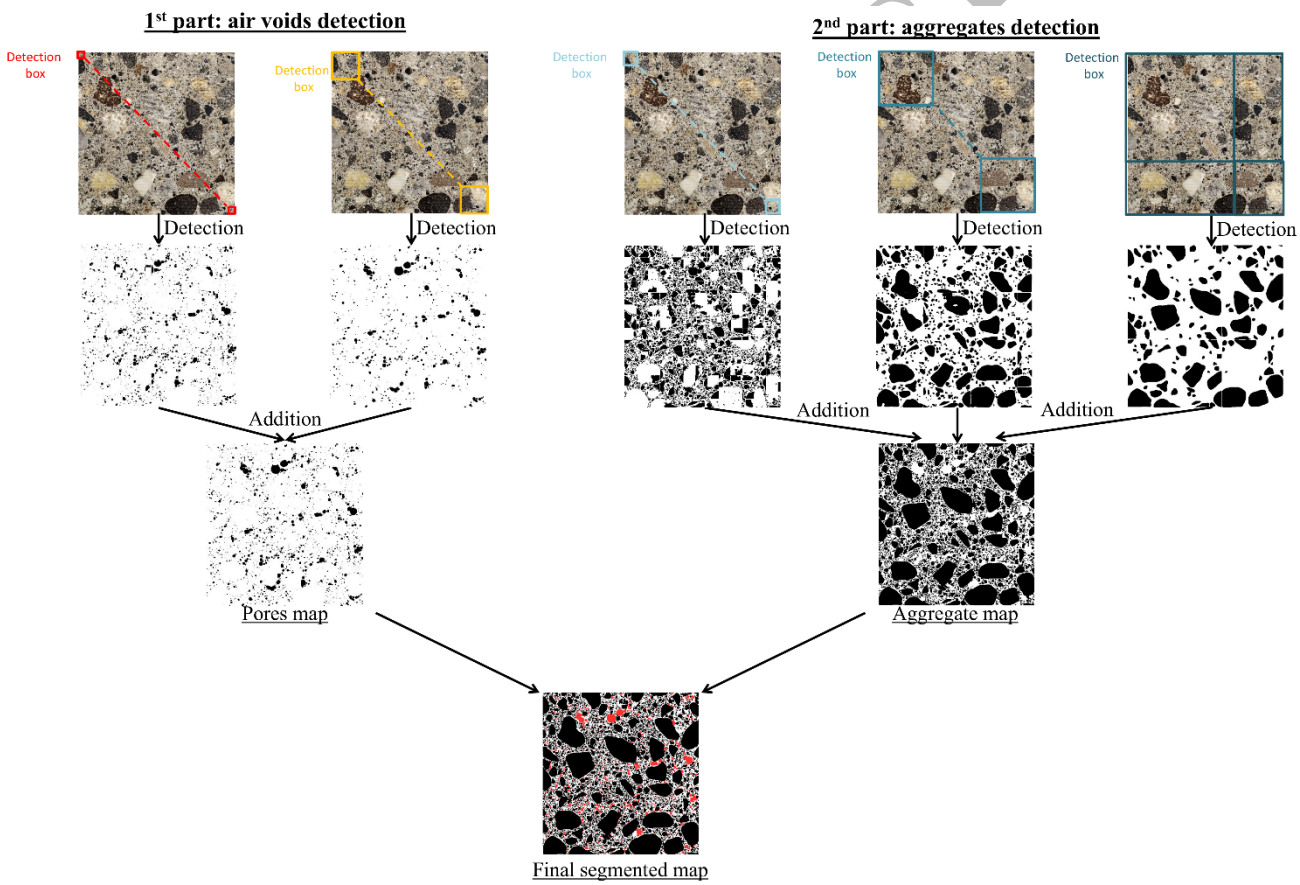

223

224 **Fig. 3.** Combination of deep learning air voids detection algorithm and deep learning
225 aggregate detection algorithm for modular deep learning instance-based concrete
226 segmentation.

2.2.2 CNN model training

Subparts with sizes of 608 x 608 pix of the raw images with a resolution divided by 2, 8 or 16 were used to train the aggregate-detection algorithm, while 608 x 608 pix subparts of the raw images with the original resolution and a resolution divided by 4 were used to train the air voids detection algorithm. Two sample datasets, containing 1470 images and 554 images, were built for the air voids detection and the aggregate detection algorithm respectively. The training dataset composition of the air voids detection model is described in Table 5. These datasets were divided into training, validation and test sets given the following proportions: 78%, 13%, 9% for the air voids detection algorithm and 56% 22% and 22% for the aggregate detection algorithm. All the images were annotated using VGG Image Annotation software [47] at an approximate pace of 50 - 100 instances per hour (total annotating time around 30 hours) by an experienced operator. Polygonal shapes were used to manually annotate the images used to train the model for aggregate detection. These annotations were divided into 'sand' and 'aggregate' based on the visual size of the elements, as illustrated in Fig. 4. Similar circular annotations were done to prepare training images for the air voids detection algorithm. These circular annotations can help the model detect air voids with similar shapes. Aggregates were annotated using polygonal shapes to help the algorithm find the air void and aggregate cutting surface. In some cases, small sand particles with a diameter smaller than 30 µm have not been annotated as the model could hardly detect them due to resolution limitations.

Table 5. Image dataset main characteristics

Specimen type	**Number of images**	**Magnifications**	**Resolutions (µm/pix)**
Cement paste 1	32	×50, ×25, ×12.5	3.13, 6.27, 12.54

Cement paste 2	19	×50, ×25, ×12.5	3.13, 6.27, 12.54
Mortar 1	210	×50, ×12.5	3.13, 6.27
Mortar 2	188	×50, ×12.5	3.13, 6.27
Concrete 1	59	×50	3.13
Concrete 2	52	×50	3.13
Concrete 3	129	×50, ×12.5	3.13, 6.27
Concrete 4	350	×50, ×25, ×12.5	3.13, 6.27, 12.54
Concrete 5	121	×50, ×25, ×12.5	3.13, 6.27, 12.54
Concrete 6	125	×50, ×25	3.13, 6.27
Concrete 7	105	×50	3.13
Concrete 8	80	×50	3.13

249

a)

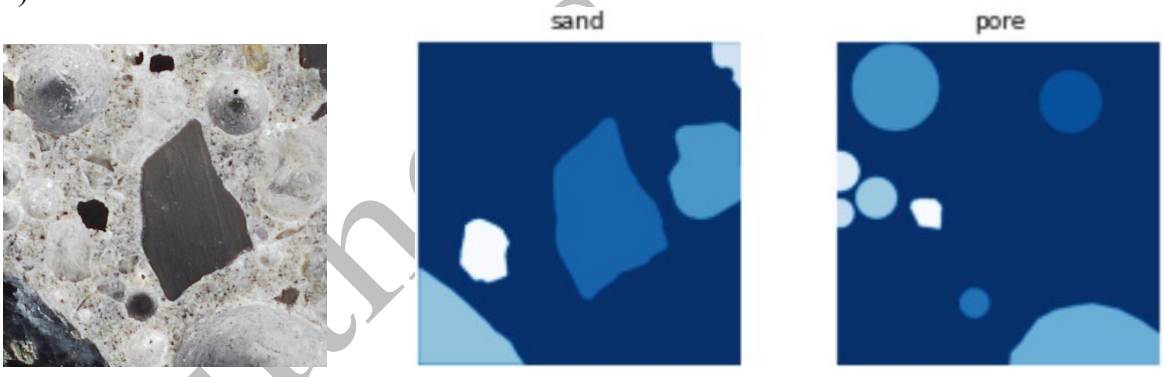

b)

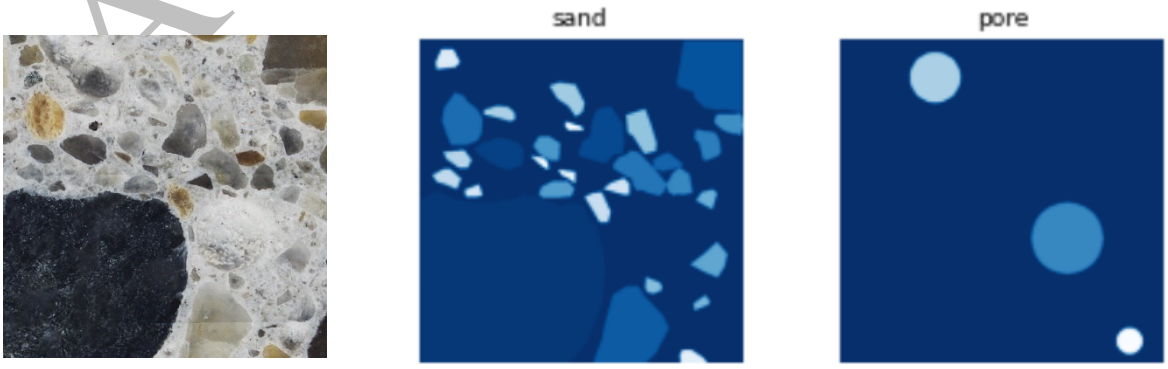

c)

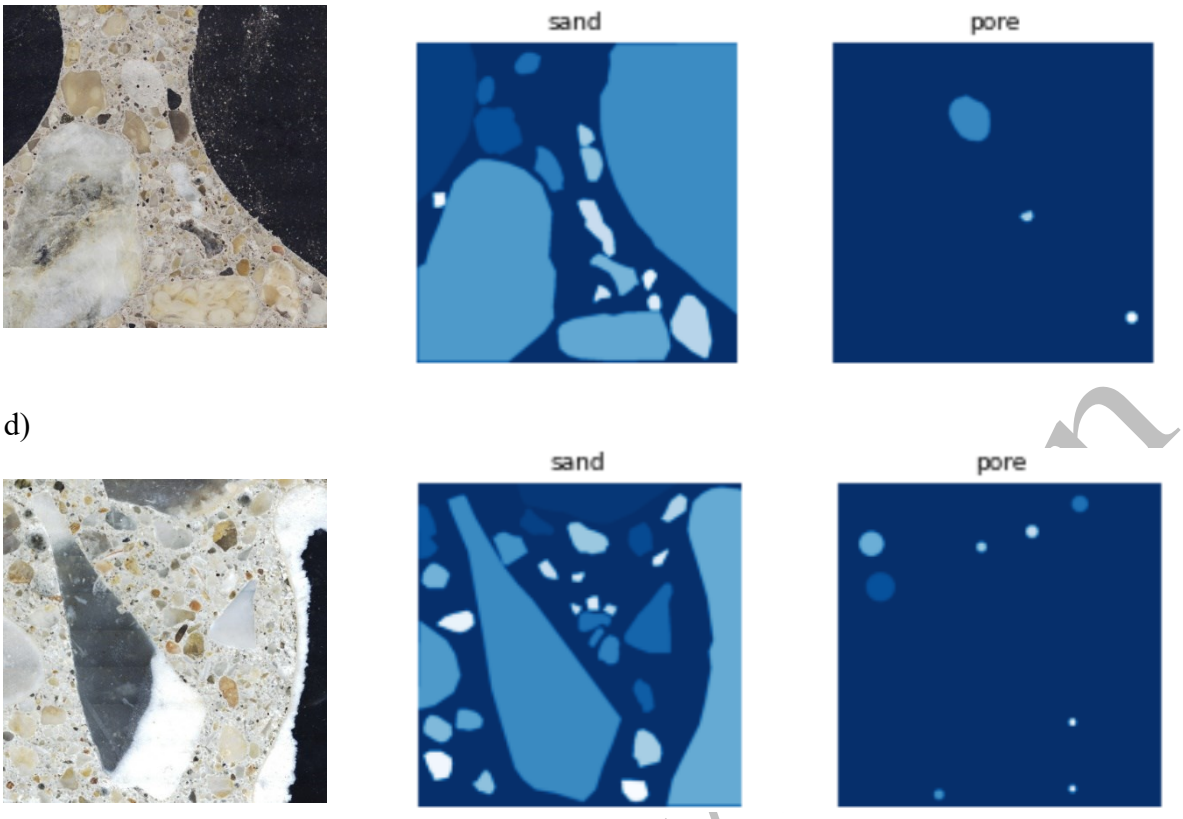

Fig. 4. Training images for the aggregates detection model (sand and aggregates in light blue shades or white and unannotated portions in dark blue)

Data augmentation has been used to generate more training images artificially. Three techniques were used in a random order using the ImgAug package [48]: horizontal flip, vertical flip, and multiplication to generate brighter or darker images.

Both models were trained using commercial GPU (Nvidia RTX 2080 Ti, 11 Go GDDR6) as follows: initial weights from COCO dataset were used then, first, during stage 1 of training, the head layers were trained during 125 epochs (250 steps/epoch) to build a good model adapted to air voids detection quickly (but not optimized regarding low-level features), then, during the stage 2 of training, all the layers except the first four were trained during 125 more epochs to tune almost all the weights of the Resnet-101 model, and finally, during the last stage, all the layers were trained during ten extras steps. The best model regarding the mean average precision (mAP) calculated on the test set was selected among the ten last ones.

264 Training parameters were adjusted to allow a fast convergence. These parameters are given in
265 Table 6.

266 **Table 6.** Training parameters of the Mask R-CNN model for aggregate and air voids detection

General parameters	**Aggregates**	**Air voids**
Batch size	4	4
Image dimension	512 x 512	512 x 512
Image resize mode	Crop	Crop
Min confidence detection	0.7	0.7
Validation steps	50	50
Learning momentum	0.9	0.9
Weight decay	0.0001	0.0001
Training stage 1		
Epochs	150	125
Steps per epoch	250	250
Learning rate	0.001	0.001
Training stage 2		
Epochs	125	500
Steps per epoch	250	250
Learning rate	0.0005	0.0005
Training stage 3		
Epochs	10	10
Steps per epoch	250	250
Learning rate	0.0001	0.0005

267

2.2.3 CNN model validation

Model results on the test images were first manually checked to assess the detection quality of hardly visible instances (small or irregular air voids, aggregates with a color similar to the surrounding cement paste, or granite aggregates with very irregular color patterns). Then, after training, mean average precisions (mAP) for IoU values between 0.5 and 0.95 (mAP @0.5-0.95) of the air voids detection algorithm and the aggregates detection algorithm were computed on test images. The general definition for the Average Precision (AP) is the area under the precision-recall curve for a given image. mAP is defined as follows:

$$mAP = \frac{\sum_{q=1}^{Q} AveP(q)}{Q} \quad (1)$$

where Q is the number of queries in the set and $AveP(q)$ is the average precision (AP) for a given query, q.

All the precision - recall curves can be generated for the test images but a more visual idea of the quality of the prediction can be obtained by plotting the predictions vs. the ground truth definition. mAP indicator has the advantage of being discriminative enough to classify modern models precisely. The intersection over union (IoU) parameter has also been calculated for some of the final models.

2.3 Protected Paste Volume (PPV) and distance-to-air-void calculation using segmented images

2.3.1 Distance-to-air-void calculation considering aggregates effect

Several algorithms were implemented in Julia language using a multi-threaded approach to analyze the high-definition pores and aggregates segmented images [49]. First, the distance between any point in the cement paste to the nearest void was calculated considering the aggregate presence. The median distance-to-air-void in the entire image was then saved in

order to be compared to experimentally measured spacing factor values. The algorithm can be summarized as follows:

-locate all the pixels at the periphery of the pore,

- compute the distance of their neighbors if they are not aggregates and select the minimum distance for each of these pixels,

- repeat the procedure using these pixels as inputs and stop when 99.5% of the distances have been found.

Several input segmented image resolution were used to find to the best compromise between precision of the calculated distances and computational time. The best results were obtained using segmented images with a resolution of 24 µm / pix and a size around 3500 x 3500 pix (raw images with a height and a width divided by 8). The distance-to-air-void calculation can be performed in approximately 100-150s using such parameters and a 10-cores commercial desktop computer.

2.3.2 Protected Paste Volume (PPV) calculation

The protected paste volume defined in [11] was calculated based on the segmented concrete images by the deep learning model. PPV represents the proportion of points in the paste for which the straight line distance to an air void is smaller than 200 µm. PPV was calculated using Julia and PPV values were saved to be compared to experimental spacing factors. High definition maps of the protected paste areas were finally generated for all the concrete samples. The number of air voids in the high definition images has been numerically calculated to complement PPV calculation by using ImageJ software.

3. Results and discussion

3.1 CNN model training results

The loss curves recorded during training are displayed in Fig. 5. A two-step decrease can be observed for both models as expected due to the first two stages during training. The loss reduction rate becomes relatively small after 300 to 400 steps (75k to 100k epochs), as the subsequent improvement could mainly be attributed to model overfitting (slow decrease of mAP calculated on the test set with increasing training). Indeed, a maximum mean average precision (mAP) (calculated on test images) of 0.5829 has been obtained after 154 steps (38.5 k epochs) for the aggregate detection model, while a maximum mAP of 0.677 has been obtained after 275 steps (68.75k epochs) for the air voids detection model. These results confirm that the Mask R-CNN model is slightly slower to train than other models[31], but the obtained mAP values are on par with precisions of around 0.65 obtained on very large datasets in image recognition reference studies [34], highlighting the potential of the model.

a)

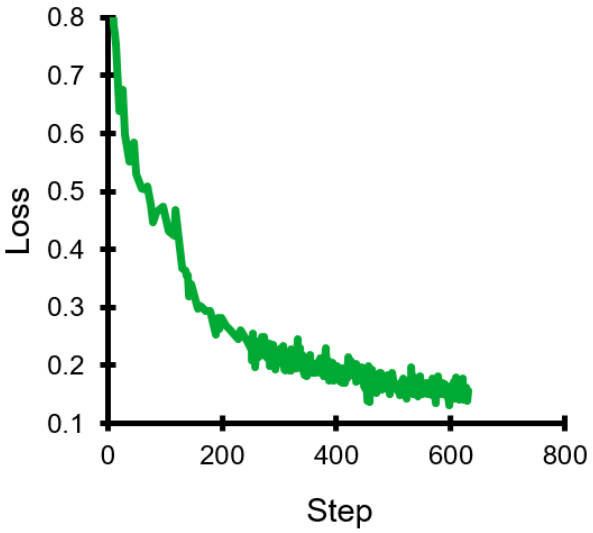

b)

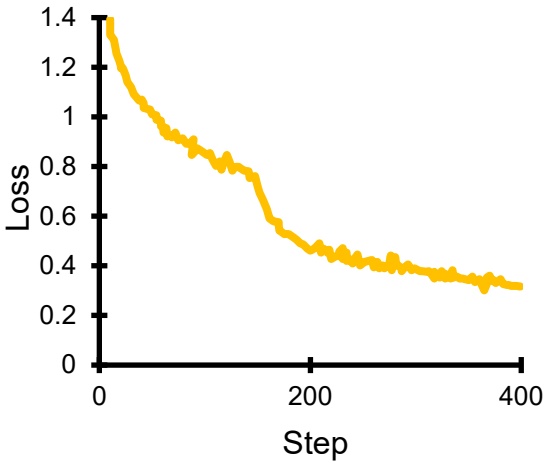

Fig. 5. Loss curves obtained during training: loss value vs step number (each step corresponds to 250 epochs) for a) the air voids detection model, and b) the aggregates detection model.

3.2 CNN model accuracy on test images

3.2.1 Results of the air voids detection model

Results of the model can be analyzed using the predictions on the test images in order to identify the most common shortcomings of the algorithm and its advantages compared to previously reported performances on similar algorithms.

Fig 6 illustrates the testing performance of the air voids detection model on 608 x 608 pix images of different mortar and concrete samples with various types of aggregates with x 50 magnification or an equivalent x 12.5 magnification (obtained dividing the size of x 50 by 4). The Mask R-CNN model performs well even in challenging situations and is able to detect the vast majority of the air voids with high confidence levels indicated by scores close to the masks in Fig. 6. As illustrated in Fig. 6.a) and 6. b) the model can detect non-circular air voids close to grey-color aggregates while a majority of the identified air voids used for training were declared of circular shape. Various air voids sizes can also be detected in the same image as illustrated by Fig. 6 c) due to an appropriate number of regions of interest (ROI)

used during training. The model is also robust regarding air voids detection in aggregates, as illustrated in Fig. 6 d) though this problem is relatively common in segmentation models previously described in the literature. Finally, because of the variety of the images in the training set, the model prediction capacity is relatively good in the case of poorly prepared images with relatively rough surfaces and illumination issues as illustrated by Fig. 6 g) and h). Last but not least, because the model is an instance-based model, it is able to distinguish very close air voids sharing some borders as exemplified by red and green air voids in Fig. 6 h). This capacity may potentially lead to a better estimation of the air voids size distribution in samples.

a)

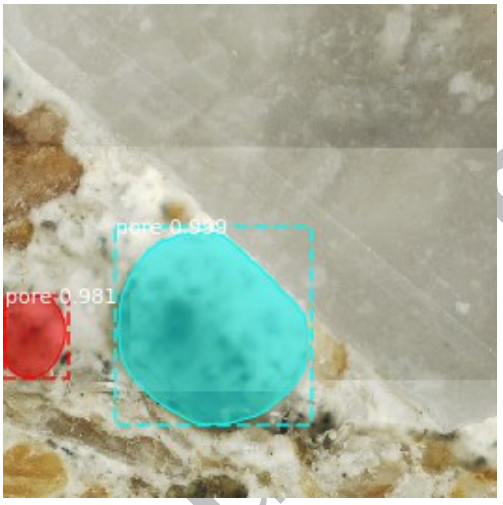

b)

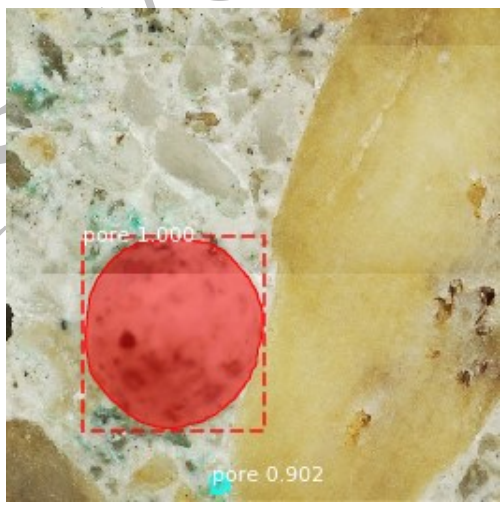

c)

d)

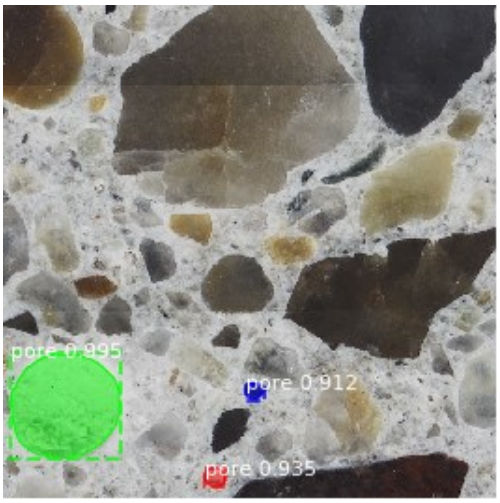

e)

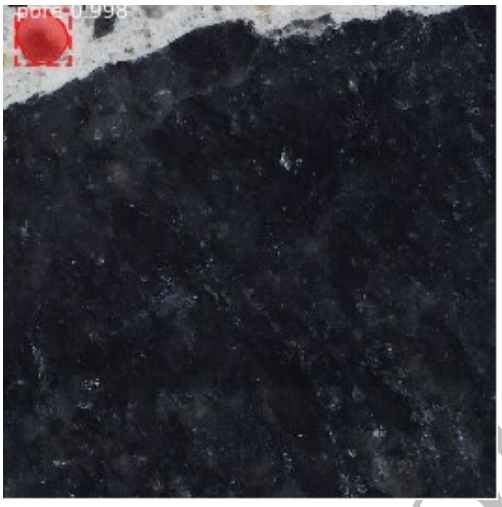

f)

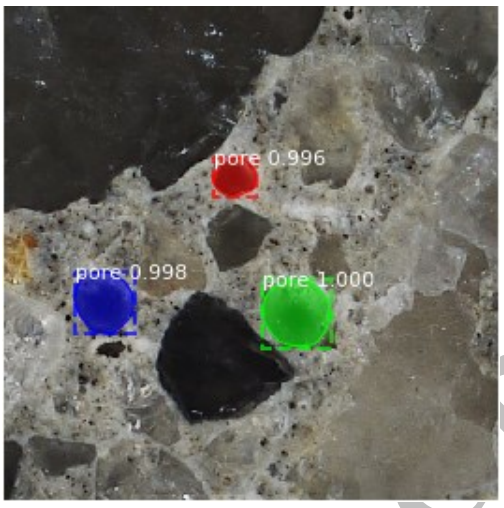

g)

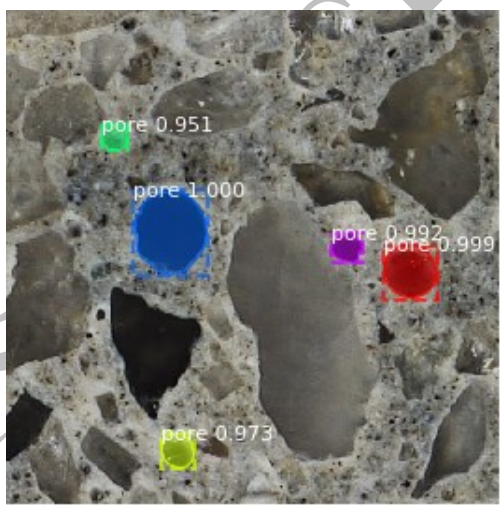

h)

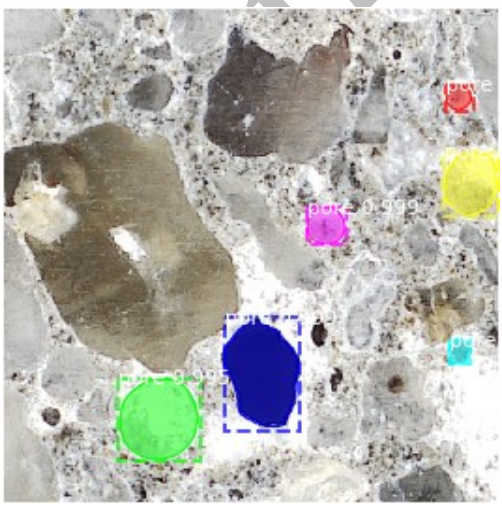

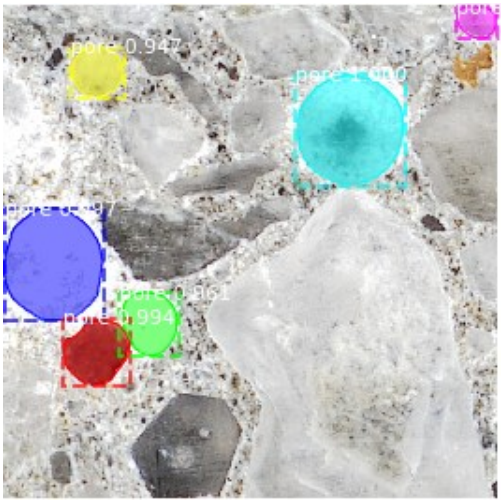

351 **Fig. 6.** Inference results of the instance segmentation model on various test images

352

The accuracy of the model can be measured using the mean average precision indicator on the test set. The general definition for the Average Precision (AP) is the area under the precision-recall curve for a given image. All the precision - recall curves can be generated for the test images, but a more visual idea of the quality of the prediction can be obtained by plotting the predictions vs the ground truth definition as illustrated in Fig. 7 As it can be seen, the predictions closely match the ground truth manual definition of the air voids leading to a good precision even at relatively high IoU values. Computing the various precisions of the prediction for IoU values between 0.5 and 0.95, an average prediction value AP @0.50-0.95 can be calculated for each image as illustrated in Table 7.

Table 7. Average precision for different IoU values for one typical test image.

Average precision at given IoU	**Value**
AP @0.50:	1.000
AP @0.55:	1.000
AP @0.60:	1.000
AP @0.65:	1.000
AP @0.70:	1.000
AP @0.75:	1.000
AP @0.80:	1.000
AP @0.85:	1.000
AP @0.90:	0.500
AP @0.95:	0.500
AP @0.50-0.95:	0.900

The final mean average precision of the model can then be calculated using the average precision of all the images. The cumulative distribution of the mAP values on the test set after 230 steps (eg 57.5 k epochs) is reported in Fig. 7 a. The model exhibits mAP value higher than 0.5 for 70% of the test images and only 13.5% of the images are associated with a mAP smaller than 0.4. After 230 training steps, a mAP value of 0.6452 is obtained over the entire test set which is on par with mAP values reported for other datasets [27].

The mean average precision obtained on the test set can be calculated depending on the duration of the training stage. As illustrated in Fig. 7 b), mAP quickly increased as the top layers of the model were trained during the first stage of training. Then, during the second stage of training (starting after 125 steps), the precision of the model initially increased until 275 training steps and a maximum mAP of 0.677 has been obtained with one model while several models exhibited mAP above 0.65 with a training duration between 230 and 2100 steps. However, with more training steps (above 300 steps), even though the loss curve decreased, mAP started decreasing slightly and dropped to values close to 0.61 after 630 training steps because of the model overfitting. Therefore, the later results about the model application will be based on the best model, considering mAP on the test set, obtained after 244 training steps in stage 1 and 2 and 2 training steps of all the model layers in step 3 (see Table 6).

a)

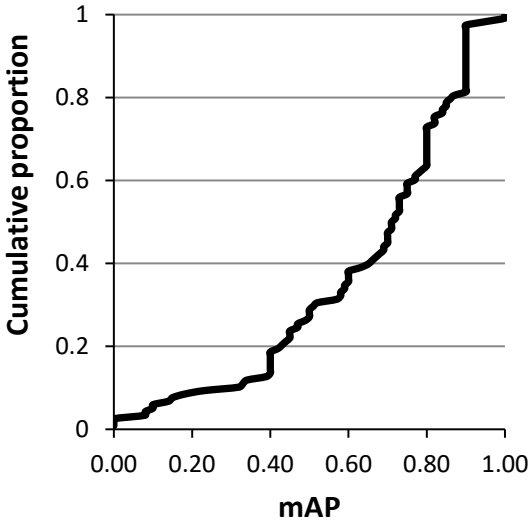

b)

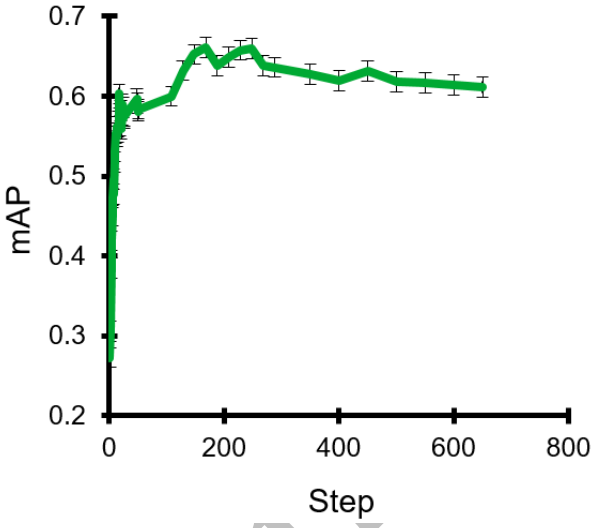

384 **Fig. 7.** Calculated mean average precisions of the model: a) typical cumulative distribution of
385 the mean average precision (mAP@0.5-0.95) over the test set after 230 training steps; b) mAP
386 on the test set depending on the training duration (1 step = 250 epochs).

387

388 3.2.2 Results of the aggregate detection model

389 Additionally, several predictions of the aggregate model have been displayed alongside
390 original 'ground truth' manual annotations in Fig. 8 for eight test images with various mAP.
391 First, it can be observed that the model correctly find the various types of aggregates in the

test images even for relatively small mAP of around 0.3 (Fig. 8 a and b), proving its versatility in detecting aggregates in a wide range of cementitious materials. The aggregate model could also detect some air voids with a relatively good precision even if the air voids specific model is more precise. Based on the analysis of the precision of the model on all the test images, it has been observed that the model exhibited very good results when the contrast between the aggregates, air voids and cement paste was high, for example in the case of light grey paste and dark aggregates.

Fig 8 a) and b) illustrate the major shortcomings of the aggregate model during detection that occur for less than 8% of test images. As illustrated in Fig. 8 a), aggregates located at the border of images or cut by the image border were likely not entirely detected, and, as shown in Fig. 8 b), small bright aggregates or sand particles inside bright cement paste could not be detected at all in images with medium magnification. The first shortcoming was effectively reduced in high-definition concrete images by selecting several image magnifications (see paragraph 2.2.1) while the second shortcoming could be eliminated using higher magnification images.

Median precision results are illustrated in Fig. 8 c) and d). These figures show that the aggregate model can detect the annotated aggregates very precisely from bright to dark aggregates, eventually with some local defects (here indentation imprints). In the mortar image, only a very limited amount of aggregates has not been found by the algorithm while, interestingly, the model correctly detected some aggregates in the normal strength concrete image even though they have not been manually annotated.

The aggregate model exhibited relatively good mAP of around 0.45 to 0.5 on ultra-high strength slag-based concrete and lightweight aggregate concrete as illustrated in Fig. 8 e) and f) respectively. Most of the basalt aggregates were detected in the ultra-high performance concrete image while some small quartz particles were not detected. Concerning the

lightweight aggregate image, the instance-segmentation model correctly captured the aggregates, both their shape and size, without being influenced by the inner porosity leading to segmented images with a clear distinction between aggregates, air voids and cement paste as opposed to pixel-based models [31].

a)

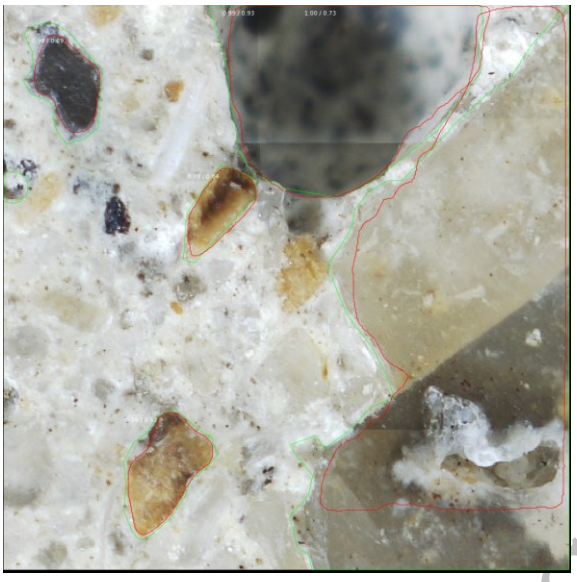

b)

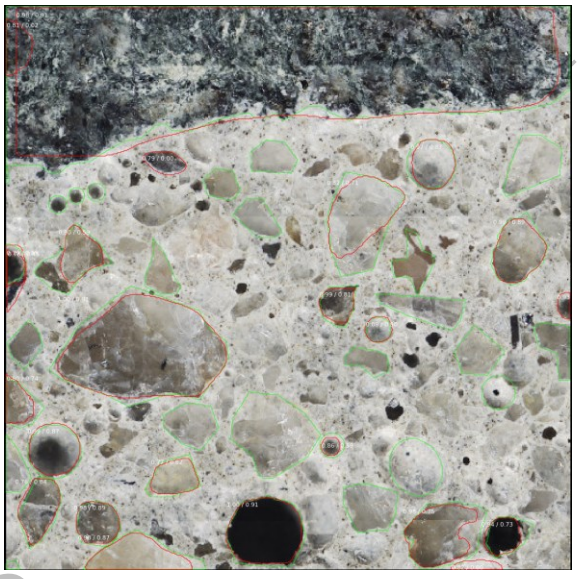

c)

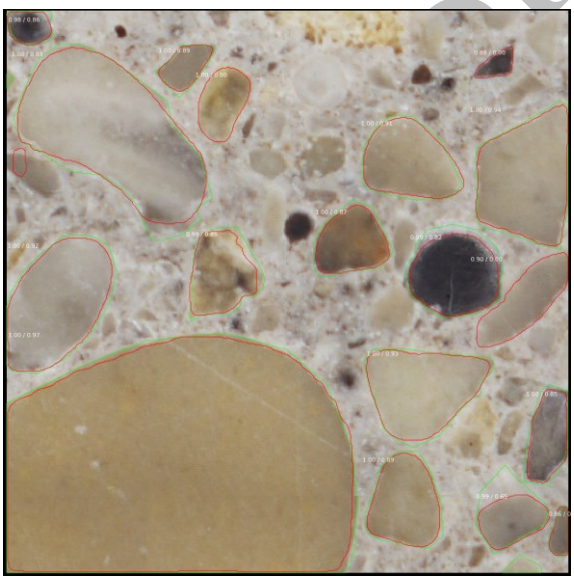

d)

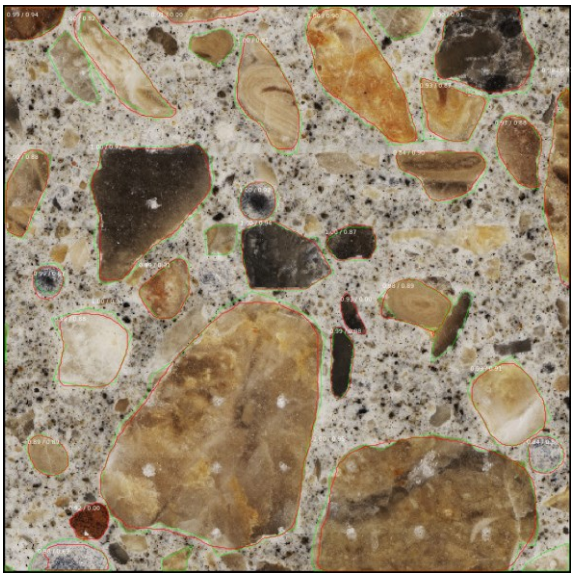

e)

f)

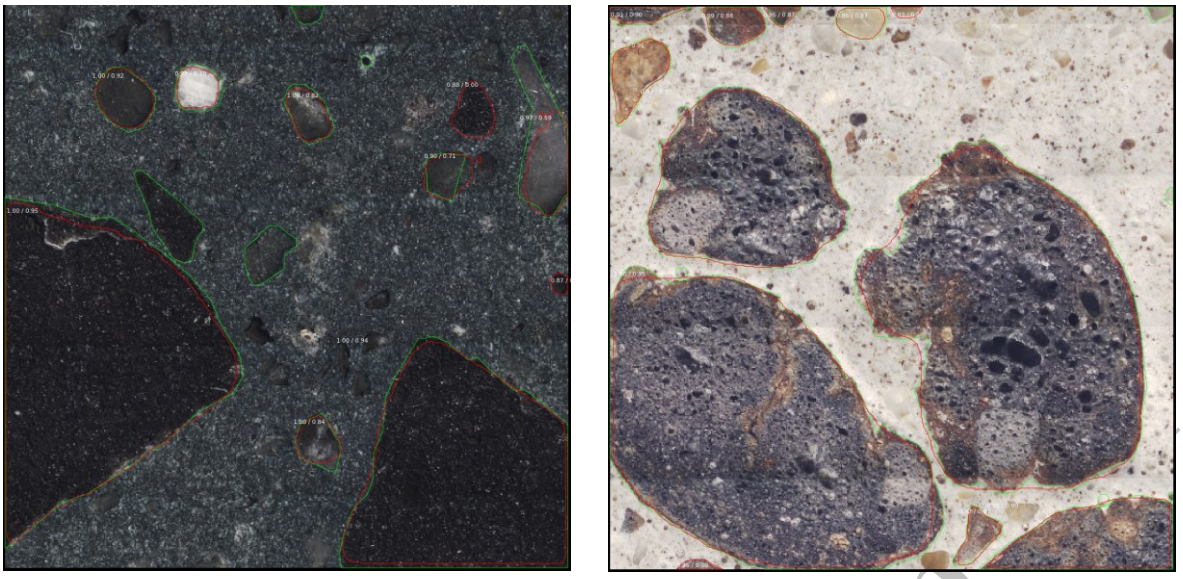

Fig 8. Typical predictions on test images with various mean average precisions (mAP): a) prediction on a ×50 normal strength concrete image with mAP 0.313; b) prediction on a ×12.5 normal strength concrete image with mAP 0.292; c) prediction on a ×50 normal strength concrete image with mAP 0.589; d) prediction on a ×50 high strength mortar image with mAP 0.571 (partly covered with indentation imprints on the bottom part); e) prediction on a ×12.5 ultra-high strength slag-blended concrete image with mAP 0.447; f) prediction on a ×12.5 lightweight aggregate concrete image with mAP 0.49 (red contours: predictions, green contours: annotations)

3.3 Application of the air voids detection model on concrete petrographic slices

Using the air voids model alone and the aforementioned strategy, the model can be applied on a wide variety of large-scale concrete petrographic slices. Fig. 9 exposes the results obtained on an unknown concrete slice from an industrial partner with a size of approximately 60 mm x 60 mm. Fig. 9 a) and b) detail the prediction results obtained in the high resolution reconstructed x 50 magnification image. As it can be seen, the model localizes various air voids of several sizes and does not predict the presence of air voids on the aggregates (even in the case of multicolored or white aggregates in the central part of the image, nor gray and

brown sand particles). However, due to the split of the images in several parts, some large air voids overlapping between several images may not be accurately detected. For this reason, the model is run on a reduced-size image as illustrated in Fig. 9 c) and d) in order to associate one instance to the largest air void. The model detects these air voids with a good accuracy but, due to the image size reduction, the model applied on a reduced-size image cannot detect the small air voids. Thus, the predicted air void content drops from 7.48 % for the full-size image to 3.94 % for the reduced-size image. However, thanks to the implemented strategy associating the detection on full-size and reduced-size image, the detection of air voids with various sizes with minimal diameters of around some pixels is possible (around 10-20 µm) and a final air void content of 7.76 % is predicted which is on par with the industrially-measured air content. Further analysis can be performed, and the algorithm's superior performance compared to manual contrast enhancement methods has been highlighted in another study [50].

a) b)

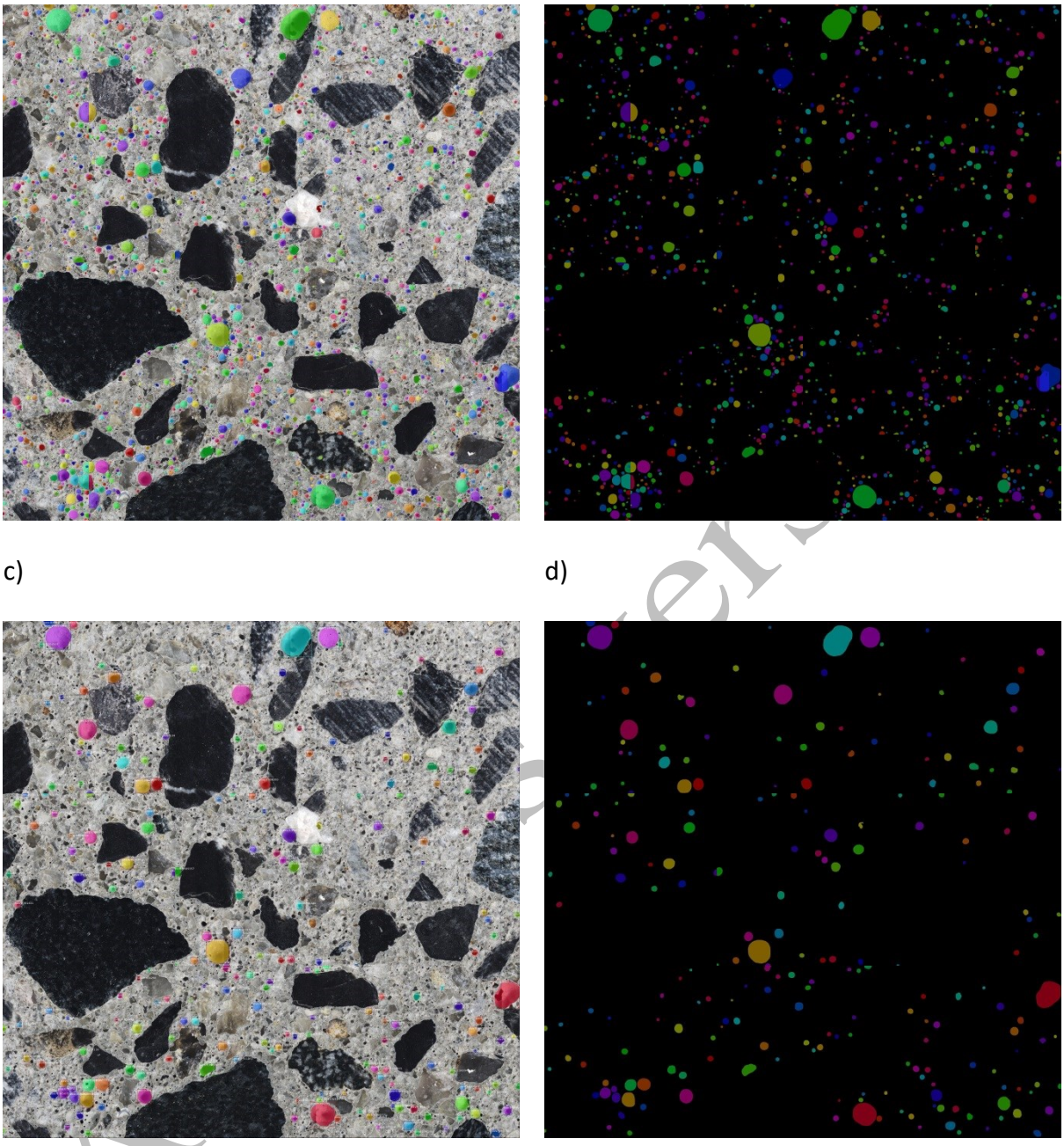

c) d)

Fig. 9. Inference result on a high-definition concrete slice image: a) full-size raw image and detected air voids instances, b) mask of the detected instances in the full-size image, c) reduced-size raw image and detected air voids instances, b) mask of the detected instances in the reduced-size image

3.4 Application of the modular deep learning model: interest of Protected Paste Volume (PPV) and distance-to-air-void calculation to assess freeze-thaw resistance

3.4.1 Modular deep learning algorithm performance and automated distance-to-air-void calculation

Combining the air voids and aggregate detection algorithms, the modular CNN model enables fast and accurate calculation of the distance of any point in the cement paste to the closest air void. The overall algorithm performance has been evaluated on concrete high-definition images. A mean mAP value of 0.66 was obtained, and the IoU calculated on several concrete images ranged from 0.855 to 0.910, highlighting outstanding results on par with pixel-based segmentation techniques.

The median distance-to-air-void has been extracted from the cumulative curves as illustrated in Fig. 10. As expected based on Power's theory, a positive correlation has been found as the median distance-to-air-void gradually increases for L factor ranging from around 130 µm to more than 430 µm. The best-fitting linear regression is found close to the identity line, demonstrating the model capacity for distance-to-air-void calculation. Interestingly, the median distance-to-air-void is found to be slightly larger than the experimentally measured L factor. This could be explained by the fact that some very small air bubbles might not have been detected as some samples with L factors smaller than 200 µm have slightly higher median distance-to-air-void, but this finding could more probably be attributed to samples with larger spacing factors (top right of the figure) as the algorithm takes into account the presence of aggregates which increase the larger distances to air voids as water should turn around the aggregate before reaching an air void. Finally, although a relatively large number of samples has been observed, it is worth noting that the 95 % confidence interval is rather extended and no clear distinction can be made between samples with spacing factors smaller than 300 µm while some of them might be frost resistant while others no. Last but not least,

481 although providing novel information and filling the gap between experimental and analytical
482 models, cumulative distribution functions calculation is computationally expensive as all the
483 distances to air voids might be calculated first. Therefore, other indicators should be found to
484 better characterize concrete samples air void structure.

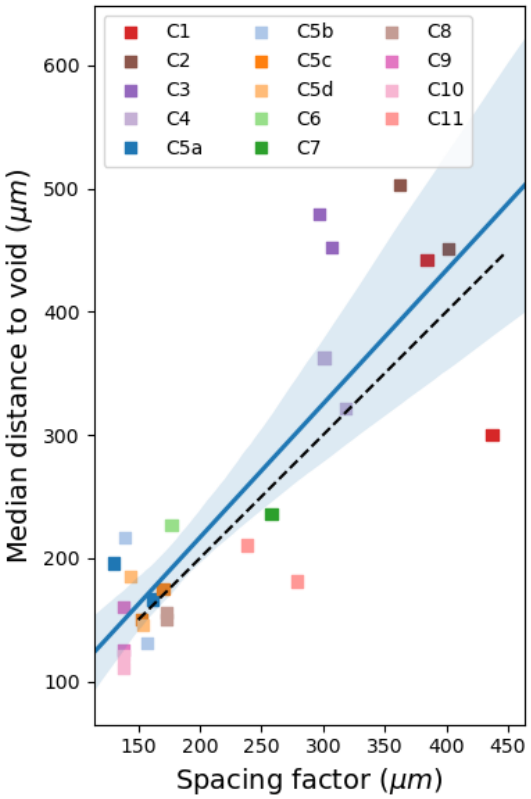

485

486 **Fig. 10.** Distance-to-air-void vs measured spacing ratio (dashed line represents identity line,
487 blue line linear regression and light blue zone 95 % confidence interval)

488

489 3.4.2 Automated Protected Paste Volume (PPV) calculation and correlation with spacing
490 factor

491 The number of air voids per unit area, which is an easily computable parameter, has been
492 compared with experimentally spacing factor for each concrete sample. As illustrated in
493 Fig. 11, the number of air voids per unit area detected by the deep learning model ranged from
494 around 0.3 air void per square millimeter to more than 1.2 air void per square millimeter on

average which illustrate the large variability of this parameter. The number of air voids per unit area exhibits an inverse correlation with the spacing factor. The correlation can be approximated by a linear regression confirming the capacity of the model to detect air voids and their critical role in the spacing factor determination. A relatively thin confidence interval has been found but the hardly physically interpretable values of the number of air voids per unit area limit the usage of this indicator.

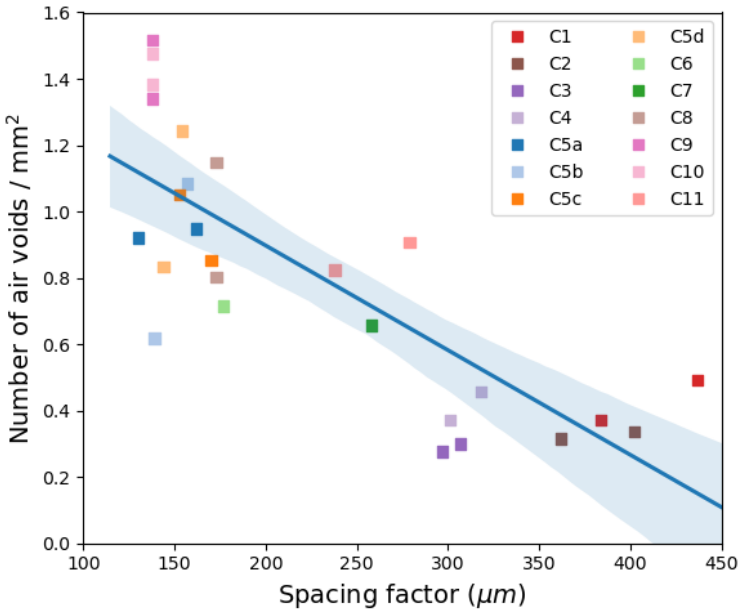

Fig. 11. Evolution of air voids content regarding experimentally measured spacing factor

For this reason, the calculation of the PPV has been performed based on the high definition segmented maps provided by the deep learning model. In Fig. 12-a), PPV has been represented regarding experimentally measured spacing factor. The calculated PPV is in good agreement with the values reported in the literature based on the measure of air voids in concrete samples prepared manually following a time-consuming procedure from the authors' opinion[11]: PPV values calculated based on the high definition images segmented using the deep learning algorithm ranged from 28% to 73%. The model is therefore able to considerably

accelerate the 2D calculation of PPV and the total computational time on a desktop computer has been measured to be around 5 to 10 minutes (including the deep learning segmentation and the multi-threaded PPV calculation). Therefore PPV can be calculated almost exclusively numerically (excepting for the polishing step of the sample) and then provide a quantitative and discriminative criteria between various concrete samples.

Numerically calculated PPV evolution regarding spacing factor has been approximated using a linear regression. Samples with spacing factors smaller than around 200 µm have been found to exhibit PPV higher than 54 % which is close to the 80% limit supposed to be freeze-thaw protective [32]. On the contrary, for samples exhibiting experimental spacing factors higher than 300 µm, calculated PPV has been found to be smaller than 43 % with some values around 30 % or less. The freeze-thaw resistance of such samples would then be relatively poor. Interestingly, a critical spacing factors range can be evidenced around 200 µm to 300 µm as the PPV abruptly drops between samples with spacing factors close to 270 µm and PPV higher than 54% and samples with spacing factors close to 290 µm with PPV smaller than 30 - 40%. Therefore, a critical attention must be paid to concrete samples with spacing factors around 200 µm to 300 µm and PPV calculation would help assessing their potential freeze-thaw resistance.

A positive correlation has been evidenced between PPV and the number of air voids per unit area as illustrated in Fig. 12-b). A linear trend can be observed for PPV smaller than 65-70%, then PPV might potentially ceil as no difference could be clearly established between samples with a high number of air void. Indeed a sample with more than 1.2 void / mm² has been found to exhibit a PPV of around 70% close to samples with a smaller number of air voids of around 1.1 void / mm². This observation confirms that overlapping air void do not increase PPV and might not lead to a better freeze-thaw resistance (while decreasing the mechanical properties).

a)

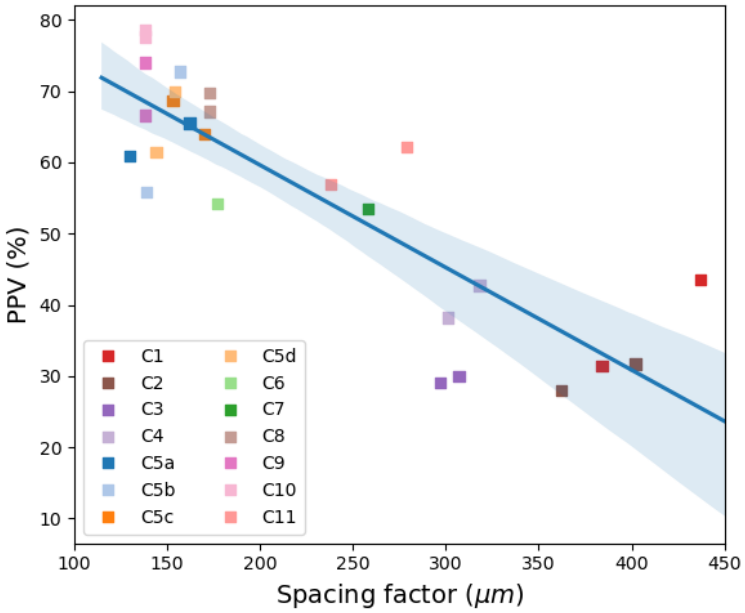

b)

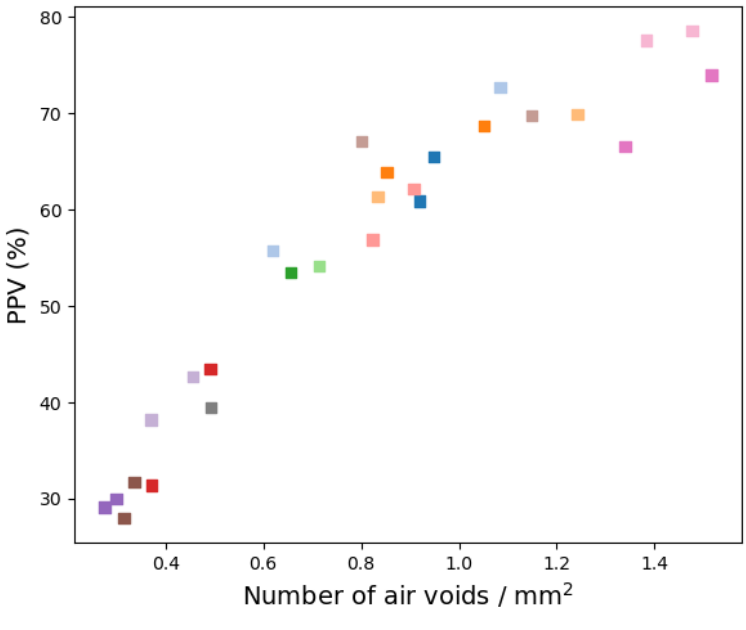

537

538 **Fig. 12.** PPV calculation of the concrete samples: a) regarding the experimental L factor, b)

539 regarding the number of air void per unit area.

540

In order to visualize protected paste regions and locate unprotected areas, high definition maps have been generated as illustrated in Fig. 13. A clear distinction can be observed between concrete samples exhibiting high and low PPV values. The extent of the green 'protected' paste considerably varies. In samples with high PPV values as illustrated in Fig 13 a), only a small portion of the cement paste cannot be considered as protected. Based on the visual observation of the generated maps, some of the unprotected zones have been located around the large aggregates confirming the importance of sand-to-aggregate ratio adjustment. Conversely, in samples with low PPV values, larger unprotected area have been found far from the large aggregates in large cement paste portions. In this case a lack of air voids in the paste, relatively far from any potentially influencing particle, might be mostly responsible of low PPV values.

a) b)

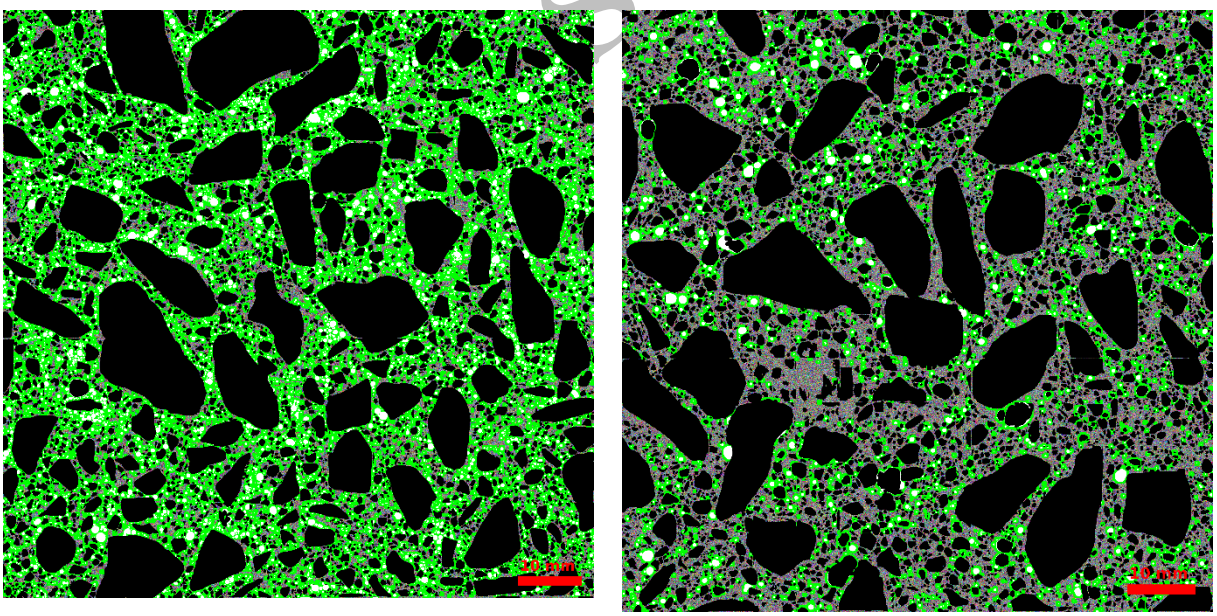

Fig. 13. Protected Paste Volume maps : a) concrete with a high PPV ratio, b) concrete with a low PPV ratio (green zone denotes the protected paste)

556 3.4.3 Comparison of experimental scaling values to numerical PPV and experimental spacing
557 factor

558 Fig. 14 represents measured scaling values of C1 to C4 concretes relatively to the numerically
559 calculated mean PPV value or to the experimentally measured mean spacing factor, both
560 calculated using two slices per concrete. It can be observed that the scaling resistance almost
561 linearly decreased as regards to the numerically calculated mean PPV values starting from
562 scaling values close to 3500 g/m² at low PPV around 30 % (C2 and C3) to 581 g/m² at
563 intermediate PPV around 40 % for C4 concrete. Interestingly, C1 concrete which included the
564 smallest amount of AEA did not generate more scaling than C2 and C3 concretes. This result
565 could have be anticipated calculating PPV value based on the microscopic images as an
566 almost linear trend has been found between numerically-calculated PPV and experimental
567 scaling values.
568 Conversely, as illustrated in Fig. 14 b, scaling values are not correlated with spacing factor for
569 C1 to C4 concrete. C1 concrete exhibited the highest spacing factor while it did not lead to the
570 highest scaling. Based on the generated PPV image, this could be due to an effective
571 repartition of the air voids in the concrete volume even though a limited amount of AEA has
572 been used. Moreover, C3 and C4 spacing factors were similar (around 310 µm) while their
573 scaling behavior was found very different. Their scaling resistance cannot be explained by the
574 experimentally spacing factor alone, while 2D-based numerically calculated PPV was found
575 sensitive to the different air void distribution which is probably influenced by the difference
576 in the maximum aggregate size in this case.
577

a)

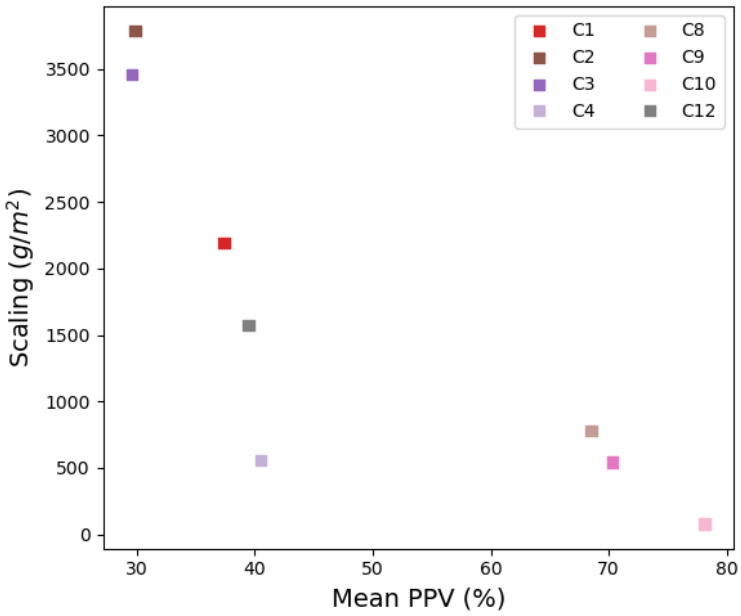

b)

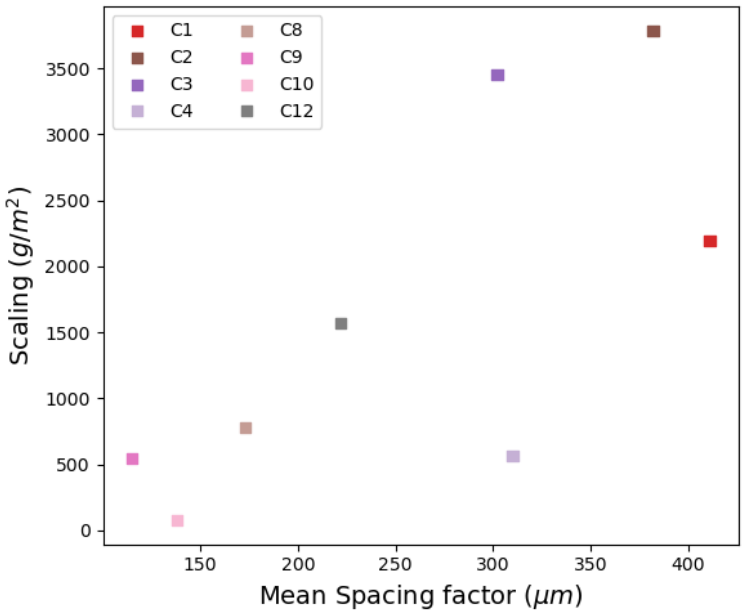

578

579 **Fig. 14.** Measured scaling values concretes relatively to: a) numerically calculated mean PPV

580 value using the deep learning algorithm, b) the experimentally measured mean spacing factor.

581

4. Conclusions

The main objective of this work was to demonstrate the potential of modular deep learning for civil engineering applications. To this end, a modular deep learning-based instance segmentation algorithm of concrete microscopic images has been developed. The algorithm is based on two CNN models dedicated to air voids and aggregate detection. Secondly, these two CNN models have been combined to perform the segmentation of high-definition concrete microscopic images. Then, the model has then been applied to freeze-thaw-related air void system characterization, namely Protected Paste Volume (PPV) and distance-to-air-void calculation. The results can be summarized as follows:

- The modular CNN model composed of two complementary Mask R-CNN architectures can be trained using distinct image sets of various magnifications.
- The model can effectively detect air voids and aggregates considering their usual shape and generate segmented images containing separated instances. Due to the region-based algorithm, segmented images correctly represent the various instances sizes and shapes because of the mask usage (conversely to pixel-level based segmentation algorithms).
- The large-scale predictions of the air voids model are in good agreement with the fresh state air void content and the ASTM 457-measured air void content due to the capacity of the model to detect both small air voids and large air voids.
- The high definition-segmented images with aggregates and air-void instances can be used to quantify 2D parameters concerning freeze-thaw resistance of concrete such as Protected Paste Volume (PPV) and distance-to-air-void. While using a modern programming language and a multi-threaded approach, these parameters can be effectively calculated on commercial computers in some minutes.

- Algorithm speed and precision facilitate the analysis of concrete sections. Based on the analysis of 20 sections, it has been shown that very good correlations can be found between the calculated 2D parameters and experimentally measured spacing factors.
- Based on the PPV calculated values, a critical spacing factor range has been evidenced around 200 µm to 300 µm. PPV can sharply decrease in this spacing factor range to around 80%, allegedly freeze-thaw protective, to around 40%, characterizing non-resistant concretes.
- Numerically calculated PPV using the modular deep learning algorithm is correlated with experimental freeze-thaw scaling resistance of moderately resistant and non-resistant concrete.

Future research directions towards improving the algorithm capabilities include the very small air voids detection and the delimitation of the small aggregates and air voids boundaries. Overall, this study might open up novel research paths regarding the potential modularity enhancement of deep learning models. Moreover, the precision of such models, which allowed a precise quantification of freeze-thaw parameters in this study, might help accelerate research towards novel findings.

Acknowledgements:

The authors would like to acknowledge Astrid-Marie Foucault, Sigma Beton (Vicat), for her help gathering information about concrete formulations.

References

[1] J.Elsena, N.Lensa, J.Vynckea, T.Aarreb, D.Quenardc, V.Smolej, Quality assurance and quality control of air entrained concrete, Cement and Concrete Research. 24 (1994) 1267–1276.
[2] T.C. Powers, A working hypothesis for further studies of frost resistance of concrete, in: Proceedings of the American Concrete Institute, 1945: pp. 245–272.

[3] T.C. Powers, Willis, T. F., The air requirement of frost resistant concrete., in: Proceedings of the Highway Research Board, 1950: pp. 184–211.
[4] M. Pigeon, P. Plante, Study of cement paste microstructure around air voids: Influence and distribution of soluble alkalies, Cement and Concrete Research. 20 (1990) 803–814. https://doi.org/10.1016/0008-8846(90)90014-O.
[5] K.A. Snyder, Numerical test of air void spacing equations, Advanced Cement Based Materials. 8 (1998) 28–44. https://doi.org/10.1016/S1065-7355(98)00007-8.
[6] D.D. Magura, Air void analyzer evaluation, Federal Highway Administration, 1996. https://rosap.ntl.bts.gov/view/dot/42581 (accessed July 30, 2021).
[7] ASTM C457 / C457M-16, Standard Test Method for Microscopical Determination of Parameters of the Air-Void System in Hardened Concrete, ASTM International, West Conshohocken, PA. (2016). https://doi.org/10/ghdg8z (accessed July 30, 2021).
[8] EN 480-11, Admixtures for concrete, mortar and grout. test methods. Determination of air void characteristics in hardened concrete, European Committee for Standardization. (2005). https://www.cstc.be/homepage/index.cfm?cat=services&sub=standards_regulations&pag=list&art=search&id=CSTC96276 (accessed July 30, 2021).
[9] J. Elsen, Automated air void analysis on hardened concrete Results of a European intercomparison testing program, Cement and Concrete Research. (2001) 5.
[10] A.-S. Dequiedt, M. Coster, L. Chermant, J.-L. Chermant, Distances between air-voids in concrete by automatic methods, Cement and Concrete Composites. 23 (2001) 247–254. https://doi.org/10.1016/S0958-9465(00)00055-X.
[11] J. Wawrzeńczyk, W. Kozak, Protected Paste Volume (PPV) as a parameter linking the air-pore structure in concrete with the frost resistance results, Construction and Building Materials. 112 (2016) 360–365. https://doi.org/10.1016/j.conbuildmat.2016.02.196.
[12] U.H. Jakobsen, C. Pade, N. Thaulow, D. Brown, S. Sahu, O. Magnusson, S. De Buck, G. De Schutter, Automated air void analysis of hardened concrete — a Round Robin study, Cement and Concrete Research. 36 (2006) 1444–1452. https://doi.org/10.1016/j.cemconres.2006.03.005.
[13] K. Peterson, J. Carlson, L. Sutter, T. Van Dam, Methods for threshold optimization for images collected from contrast enhanced concrete surfaces for air-void system characterization, Materials Characterization. 60 (2009) 710–715. https://doi.org/10/c49mwc.
[14] Y. Song, R.M. Damiani, C. Shen, D.I. Castaneda, D.A. Lange, A 3D petrographic analysis for concrete freeze-thaw protection, Cement and Concrete Research. 128 (2020) 105952. https://doi.org/10.1016/j.cemconres.2019.105952.
[15] T. Fantous, A. Yahia, Air-void characteristics in highly flowable cement-based materials, Construction and Building Materials. 235 (2020) 117454. https://doi.org/10.1016/j.conbuildmat.2019.117454.
[16] R.E. Philleo, A Method for Analyzing Void Distribution in Air-Entrained Concrete, CCA. 5 (1983) 128–130. https://doi.org/10.1520/CCA10263J.
[17] I.-C. Yeh, Modeling of strength of high-performance concrete using artificial neural networks, Cement and Concrete Research. 28 (1998) 1797–1808. https://doi.org/10.1016/S0008-8846(98)00165-3.
[18] M. Liang, Z. Chang, Z. Wan, Y. Gan, E. Schlangen, B. Šavija, Interpretable Ensemble-Machine-Learning models for predicting creep behavior of concrete, Cement and Concrete Composites. (2021) 104295. https://doi.org/10.1016/j.cemconcomp.2021.104295.
[19] B. Hilloulin, V.Q. Tran, Using machine learning techniques for predicting autogenous shrinkage of concrete incorporating superabsorbent polymers and supplementary

cementitious materials, Journal of Building Engineering. 49 (2022) 104086. https://doi.org/10.1016/j.jobe.2022.104086.
[20] F. Fueten, J. Mason, An artificial neural net assisted approach to editing edges in petrographic images collected with the rotating polarizer stage, Computers & Geosciences. 33 (2007) 1176–1188. https://doi.org/10/cr46mh.
[21] Y.J. Cha, W. Choi, O. Büyüköztürk, Deep Learning-Based Crack Damage Detection Using Convolutional Neural Networks, Computer-Aided Civil and Infrastructure Engineering. 32 (2017) 361–378. https://doi.org/10.1111/mice.12263.
[22] S. Dorafshan, R.J. Thomas, M. Maguire, Comparison of deep convolutional neural networks and edge detectors for image-based crack detection in concrete, Construction and Building Materials. 186 (2018) 1031–1045. https://doi.org/10.1016/j.conbuildmat.2018.08.011.
[23] F. Guo, Y. Qian, Y. Wu, Z. Leng, H. Yu, Automatic railroad track components inspection using real-time instance segmentation, Computer-Aided Civil and Infrastructure Engineering. (2020) mice.12625. https://doi.org/10/ghdj6k.
[24] J.D. Lau Hiu Hoong, J. Lux, P.-Y. Mahieux, P. Turcry, A. Aït-Mokhtar, Determination of the composition of recycled aggregates using a deep learning-based image analysis, Automation in Construction. 116 (2020) 103204. https://doi.org/10/ghdg8g.
[25] A.H. Rubaiyat, T.T. Toma, M. Kalantari-Khandani, S.A. Rahman, L. Chen, Y. Ye, C.S. Pan, Automatic detection of helmet uses for construction safety, in: 2016 IEEE/WIC/ACM International Conference on Web Intelligence Workshops (WIW), IEEE, 2016: pp. 135–142. https://doi.org/10/gg7wh6.
[26] W. Wilson, L. Sorelli, A. Tagnit-Hamou, Automated coupling of NanoIndentation and Quantitative Energy-Dispersive Spectroscopy (NI-QEDS): A comprehensive method to disclose the micro-chemo-mechanical properties of cement pastes, Cement and Concrete Research. 103 (2018) 49–65. https://doi.org/10.1016/j.cemconres.2017.08.016.
[27] B. Hilloulin, M. Robira, A. Loukili, Coupling statistical indentation and microscopy to evaluate micromechanical properties of materials: Application to viscoelastic behavior of irradiated mortars, Cement and Concrete Composites. 94 (2018) 153–165. https://doi.org/10.1016/j.cemconcomp.2018.09.008.
[28] B. Hilloulin, M. Lagrange, M. Duvillard, G. Garioud, ε–greedy automated indentation of cementitious materials for phase mechanical properties determination, Cement and Concrete Composites. (2022) 104465. https://doi.org/10.1016/j.cemconcomp.2022.104465.
[29] K. He, X. Zhang, S. Ren, J. Sun, Deep Residual Learning for Image Recognition, in: 2016 IEEE Conference on Computer Vision and Pattern Recognition (CVPR), IEEE, Las Vegas, NV, USA, 2016: pp. 770–778. https://doi.org/10/gdcfkn.
[30] S. Zhou, W. Sheng, Z. Wang, W. Yao, H. Huang, Y. Wei, R. Li, Quick image analysis of concrete pore structure based on deep learning, Construction and Building Materials. 208 (2019) 144–157. https://doi.org/10.1016/j.conbuildmat.2019.03.006.
[31] Y. Song, Z. Huang, C. Shen, H. Shi, D.A. Lange, Deep learning-based automated image segmentation for concrete petrographic analysis, Cement and Concrete Research. 135 (2020) 106118. https://doi.org/10.1016/j.cemconres.2020.106118.
[32] A. Molendowska, J. Wawrze, Development of the Measuring Techniques for Estimating the Air Void System Parameters in Concrete Using 2D Analysis Method, Materials. 13 (2020) 428. https://doi.org/10.3390/ma13020428.
[33] S. Liu, L. Qi, H. Qin, J. Shi, J. Jia, Path Aggregation Network for Instance Segmentation, in: 2018 IEEE/CVF Conference on Computer Vision and Pattern

Recognition, IEEE, Salt Lake City, UT, 2018: pp. 8759–8768. https://doi.org/10.1109/CVPR.2018.00913.
[34] K. He, G. Gkioxari, P. Dollár, R.B. Girshick, Mask R-CNN, in: 2017 IEEE International Conference on Computer Vision (ICCV), Venice (Italy), 2017: pp. 2980–2988. https://doi.org/10/gfghjd.
[35] B. Kim, S. Cho, Image-based concrete crack assessment using mask and region-based convolutional neural network, Struct Control Health Monit. (2019) e2381. https://doi.org/10.1002/stc.2381.
[36] N. Patel, S. Shinde, F. Poly, Automated Damage Detection in Operational Vehicles Using Mask R-CNN, in: H. Vasudevan, A. Michalas, N. Shekokar, M. Narvekar (Eds.), Advanced Computing Technologies and Applications, Springer Singapore, Singapore, 2020: pp. 563–571.
[37] P. Guo, W. Meng, Y. Bao, Automatic identification and quantification of dense microcracks in high-performance fiber-reinforced cementitious composites through deep learning-based computer vision, Cement and Concrete Research. 148 (2021) 106532. https://doi.org/10.1016/j.cemconres.2021.106532.
[38] C.V. Dung, L.D. Anh, Autonomous concrete crack detection using deep fully convolutional neural network, Automation in Construction. 99 (2019) 52–58. https://doi.org/10.1016/j.autcon.2018.11.028.
[39] Z. Liu, Y. Cao, Y. Wang, W. Wang, Computer vision-based concrete crack detection using U-net fully convolutional networks, Automation in Construction. 104 (2019) 129–139. https://doi.org/10.1016/j.autcon.2019.04.005.
[40] W. Tian, X. Cheng, Q. Liu, C. Yu, F. Gao, Y. Chi, Meso-structure segmentation of concrete CT image based on mask and regional convolution neural network, Materials & Design. 208 (2021) 109919. https://doi.org/10.1016/j.matdes.2021.109919.
[41] S. Zhao, M. Shadabfar, D. Zhang, J. Chen, H. Huang, Deep learning-based classification and instance segmentation of leakage-area and scaling images of shield tunnel linings, Struct Control Health Monit. 28 (2021). https://doi.org/10.1002/stc.2732.
[42] H. Zhang, R. Zhang, D. Sun, F. Yu, Z. Gao, S. Sun, Z. Zheng, Analyzing the pore structure of pervious concrete based on the deep learning framework of Mask R-CNN, Construction and Building Materials. 318 (2022) 125987. https://doi.org/10.1016/j.conbuildmat.2021.125987.
[43] R.-S. Lin, Y. Han, X.-Y. Wang, Macro–meso–micro experimental studies of calcined clay limestone cement (LC3) paste subjected to elevated temperature, Cement and Concrete Composites. 116 (2021) 103871. https://doi.org/10.1016/j.cemconcomp.2020.103871.
[44] C. Youssef Namnoum, B. Hilloulin, F. Grondin, A. Loukili, Determination of the origin of the strength regain after self-healing of binary and ternary cementitious materials including slag and metakaolin, Journal of Building Engineering. 41 (2021) 102739. https://doi.org/10.1016/j.jobe.2021.102739.
[45] W. Abdulla, Mask R-CNN for object detection and instance segmentation on Keras and TensorFlow, GitHub Repository. (2017). https://github.com/matterport/Mask_RCNN (accessed July 30, 2021).
[46] B. Hilloulin, Concrete Deep Segmentation, (2021). https://git.gem.ec-nantes.fr/bhilloul/concrete-deep-segmentation (accessed March 10, 2022).
[47] A. Dutta, A. Zisserman, The VIA Annotation Software for Images, Audio and Video, in: Proceedings of the 27th ACM International Conference on Multimedia, Association for Computing Machinery, New York, NY, USA, 2019: pp. 2276–2279. https://doi.org/10/ggk524.

[48] A.B. Jung, K. Wada, J. Crall, S. Tanaka, J. Graving, C. Reinders, S. Yadav, J. Banerjee, G. Vecsei, A. Kraft, Z. Rui, J. Borovec, C. Vallentin, S. Zhydenko, K. Pfeiffer, B. Cook, I. Fernández, F.-M. De Rainville, C.-H. Weng, A. Ayala-Acevedo, R. Meudec, M. Laporte, others, ImgAug, (2021). https://github.com/aleju/imgaug (accessed July 30, 2021).

[49] J. Bezanson, A. Edelman, S. Karpinski, V.B. Shah, Julia: A Fresh Approach to Numerical Computing, SIAM Rev. 59 (2017) 65–98. https://doi.org/10.1137/141000671.

[50] B. Hilloulin, I. Bekrine, E. Schmitt, A. Loukili, Open-source deep learning-based air-voids detection algorithm for concrete microscopic images, Journal of Microscopy. (2022) jmi.13098. https://doi.org/10.1111/jmi.13098.